PAPER • OPEN ACCESS

Time-resolved 3D imaging of ultrafast spin–orbit wave packet dynamics

View the article online for updates and enhancements.

New Journal of Physics

The open access journal at the forefront of physics

PAPER

CrossMark

Time-resolved 3D imaging of ultrafast spin–orbit wave packet dynamics

Tim Bayer, Daniela Gräfing, Stefanie Kerbstadt, Dominik Pengel, Kevin Eickhoff, Lars Englert and Matthias Wollenhaupt

Carl von Ossietzky Universität Oldenburg, Institut für Physik, Carl-von-Ossietzky-Straße 9-11, D-26129 Oldenburg, Germany

E-mail: matthias.wollenhaupt@uni-oldenburg.de

Abstract

We combine bichromatic polarization pulse shaping with photoelectron imaging tomography for time-resolved spatial imaging of ultrafast spin–orbit wave packet (SOWP) dynamics in atoms. Polarization-shaped two-color pump-probe sequences are generated by spectral amplitude and phase modulation of a femtosecond input pulse and used to excite SOWPs in the potassium $4p$ fine-structure doublet. By selecting different spectral bands for pump and probe pulse, we achieve interference-free detection of the spatiotemporal SOWP dynamics. Using tomographic techniques, we reconstruct the three-dimensional photoelectron momentum distribution (3D-ED) created by the probe pulse. Time-resolved measurement of the 3D-ED reveals the orbital realignment dynamics induced by spin–orbit interaction in the neutral atom.

1. Introduction

Nowadays, pump-probe techniques are established experimental tools to observe the motion of electrons and nuclei on their intrinsic ultrafast timescales. In a nutshell, a first ultrashort laser pulse (pump) initiates a quantum-dynamical process which is interrogated after a variable time delay by a second pulse (probe) mapping the dynamics onto an observable. Recently, pump-probe schemes have been employed in numerous time-resolved experiments to reveal photochemical dynamics in molecules on the pico- to femtosecond timescale, as reviewed for example in [1–3], and even faster electron dynamics in atoms on sub-femtosecond to attosecond timescales (see e.g. [4–9] and references therein). Traditionally, pump-probe pulse sequences are produced using an interferometer to create two time-delayed replica of the input pulse from an ultrafast laser source. In single-color schemes, the signals generated by pump and probe pulse often interfere in the measured spectra which complicates the signal analysis and interpretation. In contrast, two-color schemes allow to disentangle the pump and the probe step providing more specific information and enabling background-free detection of the laser-induced dynamics. An even higher degree of control is attained by using polarization-shaped laser pulses to exploit the vectorial character of light–matter interactions [10]. By adapting the polarization to the induced dynamics, both the pump and the probe step can be optimized to obtain additional information on the process under investigation [11]. Besides refined excitation schemes, the level of detail of the physical picture depends crucially on the applied detection technique. In comparison to the detection of photons, the measurement of photoelectrons benefits from high detection efficiency. Employing energy-resolved photoelectron spectroscopy already yields a wealth of dynamical information [12, 13]. Making use of angle-resolved techniques, such as velocity map imaging (VMI) [14] or cold target recoil ion momentum spectroscopy [15], reveals vectorial information in addition. In particular, angle-resolved detection schemes provide access to the dynamics of angular momenta essential to understanding spatial aspects and the emergence of directionality in photophysical and photochemical processes [16]. Eventually, a comprehensive physical picture is obtained by measurement of the full three-dimensional (3D) photoelectron momentum distribution, e.g. using tomographic techniques [17, 18].

In this contribution, we present a technique for time-resolved 3D reconstruction of ultrafast quantum dynamics by combining the aforementioned advantages of polarization-shaped pulses and highly differential photoelectron detection. The technique is based on the combination of bichromatic polarization pulse shaping, for the generation of polarization-shaped two-color pump-probe pulse sequences, with photoelectron imaging tomography to reconstruct the full energy and angular distribution of photoelectron wave packets released by the probe [19–21]. The experimental scheme has been introduced in [20] and applied to the coherent control of photoelectron momentum distributions aiming at the design of unusual angular momentum superposition states. Here, we demonstrate the power of the method to observe ultrafast dynamics and determine atomic and molecular properties. We exemplify the bichromatic pump-probe technique on a well-established model system by imaging the dynamics of ultrafast spin–orbit wave packets (SOWPs) in potassium atoms. SOWPs, being a prototype example of coherent electron dynamics, were among the first electron wave packets studied in real-time. For example, SOWPs have been investigated in Rydberg atoms on the picosecond timescale [22–24] and in alkali metals [11, 25] and noble gases [26–28] on the femtosecond timescale. Recently, the sub-femtosecond motion of SOWPs in krypton ions was observed using attosecond transient absorption spectroscopy [29]. In addition, coherent control of SOWPs based on shaped femtosecond laser pulses was demonstrated [28, 30–32] and the polarization dependence of SOWPs was studied experimentally [11, 24] and proposed as a means to produce highly spin-polarized electrons [33, 34]. So far, the dynamics of SOWPs have mainly been studied by means of scalar observables. For example, in [11, 25, 35], oscillations in the ion yield from multiphoton-ionization of potassium atoms due to variation of the ionization probability during the SOWP time evolution were measured and analyzed in a bright-/dark-state formalism. However, since SO interaction induces a precession of the electron orbital alignment in angular direction [11, 24, 33], highly differential detection techniques are required to gain a complete spatiotemporal picture of the coupled angular momentum dynamics. In [26], photoelectron imaging spectroscopy was used to observe the angular dynamics of a SOWP in krypton atoms from linearly polarized excitation and ionization. In this case, the photoelectron momentum distribution could be retrieved via Abel inversion due to its cylindrical symmetry. In general, electron wave packets created by polarization-shaped laser pulses evolving under angular momentum coupling are not necessarily symmetric. Below, we present the first 3D tomographic reconstruction of ultrafast SOWPs in the potassium $4p$ fine structure doublet and track their orbital alignment in time. After the excitation by the pump, the observed wave packet dynamics is solely related to spin–orbit (SO) interaction which raises the degeneracy of the $4p$ state. The oscillation period $T = h/\Delta\varepsilon$, where $\Delta\varepsilon$ is the fine structure splitting, is directly related to the SO interaction strength. The resulting wave packet motion can be interpreted as the precession of spin and orbital angular momentum about the total angular momentum [25]. In our experiment, the effect of the SO precession is mapped into the 3D photoelectron momentum distribution by the probe and measured using photoelectron imaging techniques. Two prototypical scenarios based on circularly and linearly polarized pump pulses are investigated. Circularly polarized excitation of the SOWP generally induces an anisotropic polarization of the atom [11], whereas linearly polarized excitation creates a symmetric state with vanishing net polarization. In the circularly polarized case, we use a counterrotating circularly polarized (CRCP) probe pulse to demonstrate the capabilities of polarization-shaped pump-probe sequences. In the linearly polarized case, we use an orthogonal linearly polarized (OLP) probe pulse specifically adapted to the orbital alignment of the SOWP at half the oscillation period [11]. Because bichromatic OLP fields are not circularly symmetric, tomographic techniques are employed to reconstruct the 3D photoelectron density. Both scenarios exhibit common underlying neutral dynamics which manifest in a counterintuitive rotation of the SOWP from its initial alignment in the laser polarization plane to an alignment coplanar to the laser propagation direction ($\boldsymbol{k}$). In the CRCP scenario, the orbital realignment of the SOWP is indicated by a change in the m_ℓ-character, m_ℓ being the orbital magnetic quantum number of the measured photoelectron wave packet. In the OLP scenario, the rotation of the neutral electron wave packet is mapped by a similar rotation of the photoelectron momentum distribution about an axis orthogonal to both the laser polarization vector ($\boldsymbol{e}$) and the wave vector, i.e. about $\boldsymbol{e} \times \boldsymbol{k}$.

The paper is organized as follows. In section 2, we introduce the physical system and develop an intuitive physical model to describe the angular distribution of photoelectron wave packets created in the experiment by the probe pulse. Section 3 introduces the experimental strategy. Experimental results from pump-probe studies of SOWPs in the potassium $4p$ fine-structure states using CRCP and OLP bichromatic pulse sequences are presented and discussed in section 4. Section 5 concludes the paper and gives a brief outlook on future perspectives of the shaper-based bichromatic pump-probe imaging technique.

2. Physical model

In this section, we introduce the two-color pump-probe scheme to excite and probe ultrafast SOWP dynamics in potassium atoms by polarization-shaped bichromatic pulse sequences. We start in section 2.1 by describing the
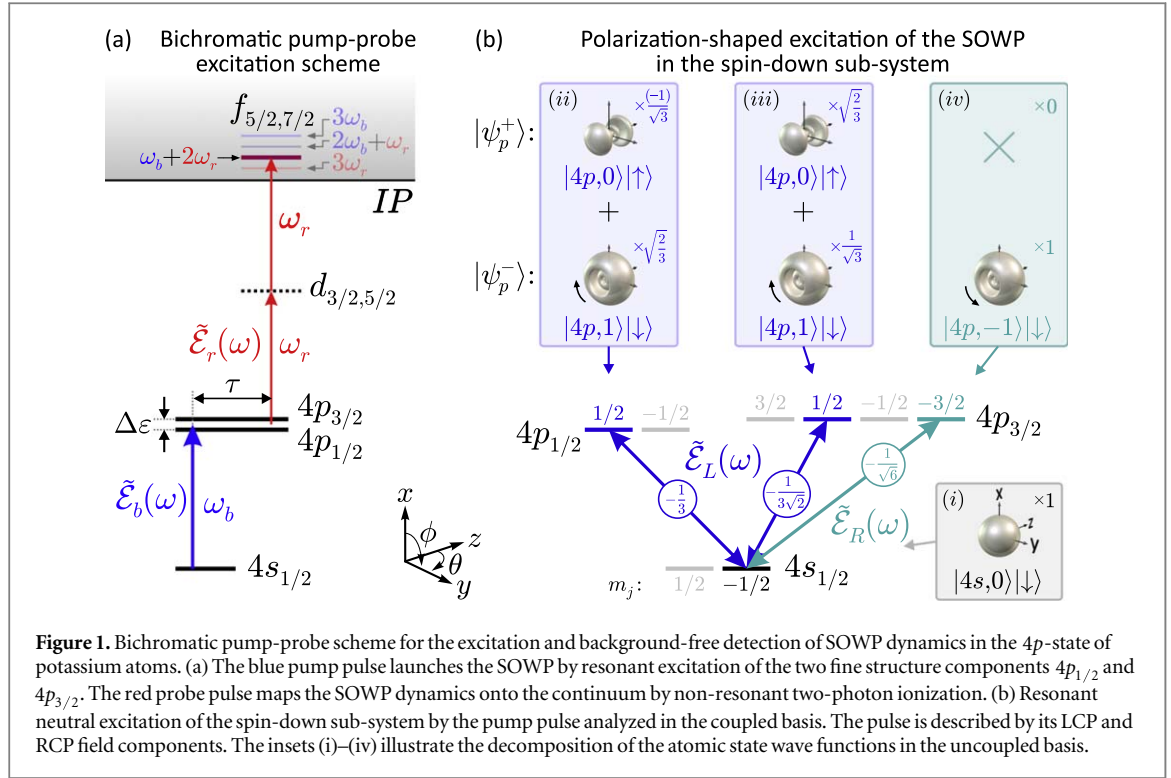
Figure 1. Bichromatic pump-probe scheme for the excitation and background-free detection of SOWP dynamics in the $4p$-state of potassium atoms. (a) The blue pump pulse launches the SOWP by resonant excitation of the two fine structure components $4p_{1/2}$ and $4p_{3/2}$. The red probe pulse maps the SOWP dynamics onto the continuum by non-resonant two-photon ionization. (b) Resonant neutral excitation of the spin-down sub-system by the pump pulse analyzed in the coupled basis. The pulse is described by its LCP and RCP field components. The insets (i)–(iv) illustrate the decomposition of the atomic state wave functions in the uncoupled basis.

shaped laser field and the excitation and ionization scheme. A detailed theoretical description of the SOWP dynamics induced in the potassium $4p$ fine-structure states by the polarization-shaped pump is given in appendix. The treatment is similar to the formalism used e.g. in [24, 26] and the bright-/dark-state model employed in [11, 25, 35]. However, the description presented here is specifically adapted to the creation of SOWPs by general polarization-shaped bichromatic laser fields and, moreover, includes the spatial aspects of the SOWP mapped into the 3D photoelectron momentum distribution. The photoionization probe step is addressed in section 2.2, where we introduce an intuitive physical model to rationalize the shape of the measured photoelectron wave packets.

2.1. Physical system

The excitation scheme of potassium atoms, interacting perturbatively with a polarization-shaped bichromatic pump-probe sequence, is depicted in figure 1(a). The sequence consists of a blue i.e. high-frequency pump pulse $\tilde{\boldsymbol{\mathcal{E}}}_b(\omega)$ followed by a red i.e. low-frequency probe pulse $\tilde{\boldsymbol{\mathcal{E}}}_r(\omega)$ at a variable time delay τ. The center frequency $\omega_b = 2.45$ rad fs^{-1} ($\lambda_b = 769$ nm) of the pump pulse is tuned to the fine structure resonances $4s_{1/2} \to 4p_{1/2}$ and $4s_{1/2} \to 4p_{3/2}$ at frequencies $\omega_{1/2} = 2.446$ rad fs^{-1} and $\omega_{3/2} = 2.457$ rad fs^{-1}, respectively, to resonantly launch the SOWP. The spectral bandwidth $\Delta\omega = 35$ mrad fs^{-1} [20] of both colors is much larger than the fine structure splitting $\Delta\varepsilon/\hbar = 7.2$ meV$/\hbar = 10.9$ mrad fs^{-1} of the potassium $4p$-state, in order to (i) couple both resonances with approximately the same field amplitude $\tilde{\mathcal{E}}_b(\omega_{1/2}) \approx \tilde{\mathcal{E}}_b(\omega_{3/2})$ and (ii) ensure that the corresponding pulse duration $\Delta t = 80$ fs is much smaller than the SOWP oscillation period $T = h/\Delta\varepsilon = 578$ fs.

By decomposing the laser electric field of the pump into a left-handed circularly polarized (LCP) component $\tilde{\mathcal{E}}_L(\omega)$ and a right-handed circularly polarized (RCP) component $\tilde{\mathcal{E}}_R(\omega)$, we allow for pump pulses with variable states of polarization. With the spherical unit vectors $\boldsymbol{e}_1 = -(\boldsymbol{e}_x + \mathrm{i}\boldsymbol{e}_y)/\sqrt{2}$ and $\boldsymbol{e}_{-1} = (\boldsymbol{e}_x - \mathrm{i}\boldsymbol{e}_y)/\sqrt{2}$ to describe LCP and RCP polarization, where $\boldsymbol{e}_{x/y}$ are the cartesian unit vectors, the polarization-shaped pump is hence written as

$$\tilde{\boldsymbol{\mathcal{E}}}_b(\omega) = \tilde{\mathcal{E}}_L(\omega)\boldsymbol{e}_1 + \tilde{\mathcal{E}}_R(\omega)\boldsymbol{e}_{-1}. \tag{1}$$

The red probe pulse projects the SOWP dynamics onto the ionization continuum via two-photon ionization from the excited $4p$-state, as depicted in figure 1(a). Its center frequency $\omega_r = 2.28$ rad/fs ($\lambda_r = 826$ nm) is detuned sufficiently far from resonance such that the probe pulse is fully non-resonant with respect to both $4s \to 4p$ transitions. The released photoelectron wave packets carry a kinetic energy of about $\varepsilon_1 = \hbar(\omega_b + 2\omega_r) - \varepsilon_{\mathrm{ip}}$, where $\varepsilon_{\mathrm{ip}}$ denotes the atomic ionization potential. For simplicity, only ionization pathways leading to an f-type continuum (via a d-type intermediate state) are indicated in figure 1(a). Additional pathways to a p-type continuum (via s- and d-type intermediates) are not shown but included in the numerical

simulations presented in section 4 (see figures 5 and 6). Even though these pathways are typically less efficient due to propensity rules [36, 37], the photoelectron wave packet is, in general, described by a coherent superposition of a *p*- and an *f*-wave [20, 21, 38].

Resonance-enhanced three-photon ionization by the blue ($3\omega_b$) and non-resonant three-photon ionization by the red pulse ($3\omega_r$) also contribute to the generated photoelectron wave packet at kinetic energies $\varepsilon_3 = 3\hbar\omega_b - \varepsilon_{\mathrm{ip}}$ and $\varepsilon_0 = 3\hbar\omega_r - \varepsilon_{\mathrm{ip}}$, respectively. In addition, when both colors overlap in time ($|\tau| \lesssim \Delta t$), intra-pulse frequency mixing by simultaneous absorption of two blue and one red photon contributes at $\varepsilon_2 = \hbar(2\omega_b + \omega_r) - \varepsilon_{\mathrm{ip}}$. However, only the photoelectron wave packet at ε_1 is sensitive to the time evolution of the SOWP, while the other three contributions are either τ-independent (ε_0 and ε_3) or vanish for time-delays exceeding the pulse duration (ε_2) [20]. Thus, by energetic disentanglement of the different photoionization channels, the bichromatic pump-probe technique allows for background-free detection of the SOWP dynamics mapped into the ε_1-channel.

Figure 1(b) displays a detailed scheme for the neutral excitation of the SOWP by the polarization-shaped pump pulse $\tilde{\boldsymbol{\mathcal{E}}}_b(\omega)$ (see equation (1)). In the coupled basis, the atomic system splits into two sub-systems characterized by the two ground states $|4s_{1/2}, -1/2\rangle$ (spin-down) and $|4s_{1/2}, 1/2\rangle$ (spin-up). The gaseous sample used in the experiment is described by a mixture of atoms being in either the spin-down or the spin-up ground state. Since the two sub-systems are completely decoupled, i.e. no dipole-allowed inter-system transitions exist, we focus on the spin-down sub-system in figure 1(b). The treatment of the spin-up sub-system is fully analogous. According to the dipole selection rules $\Delta\ell = \pm 1, \Delta j = 0, \pm 1$ and $\Delta m_j = \pm 1$ for optical transitions (see equation (A.5)), the resonant pump pulse couples the ground state $|4s_{1/2}, -1/2\rangle$ with the excited states $|4p_{1/2}, 1/2\rangle, |4p_{3/2}, 1/2\rangle$ and $|4p_{3/2}, -3/2\rangle$. As shown in figure 1(b), the transitions $|4s_{1/2}, -1/2\rangle \rightarrow |4p_{1/2}, 1/2\rangle$ and $|4s_{1/2}, -1/2\rangle \rightarrow |4p_{3/2}, 1/2\rangle$ with $\Delta m_j = 1$ are driven by the LCP field $\tilde{\boldsymbol{\mathcal{E}}}_L(\omega)$, whereas the transition $|4s_{1/2}, -1/2\rangle \rightarrow |4p_{3/2}, -3/2\rangle$ with $\Delta m_j = -1$ is driven by the RCP field $\tilde{\boldsymbol{\mathcal{E}}}_R(\omega)$. The relative dipole couplings of each transition, given in the circles, are calculated using equation (A.5). The insets (i)–(iv) visualize the decomposition of the excited atomic states in the uncoupled basis. A complete description of the resulting SOWP wave function is provided in appendix along with a discussion of SOWPs from circularly and linearly polarized excitation.
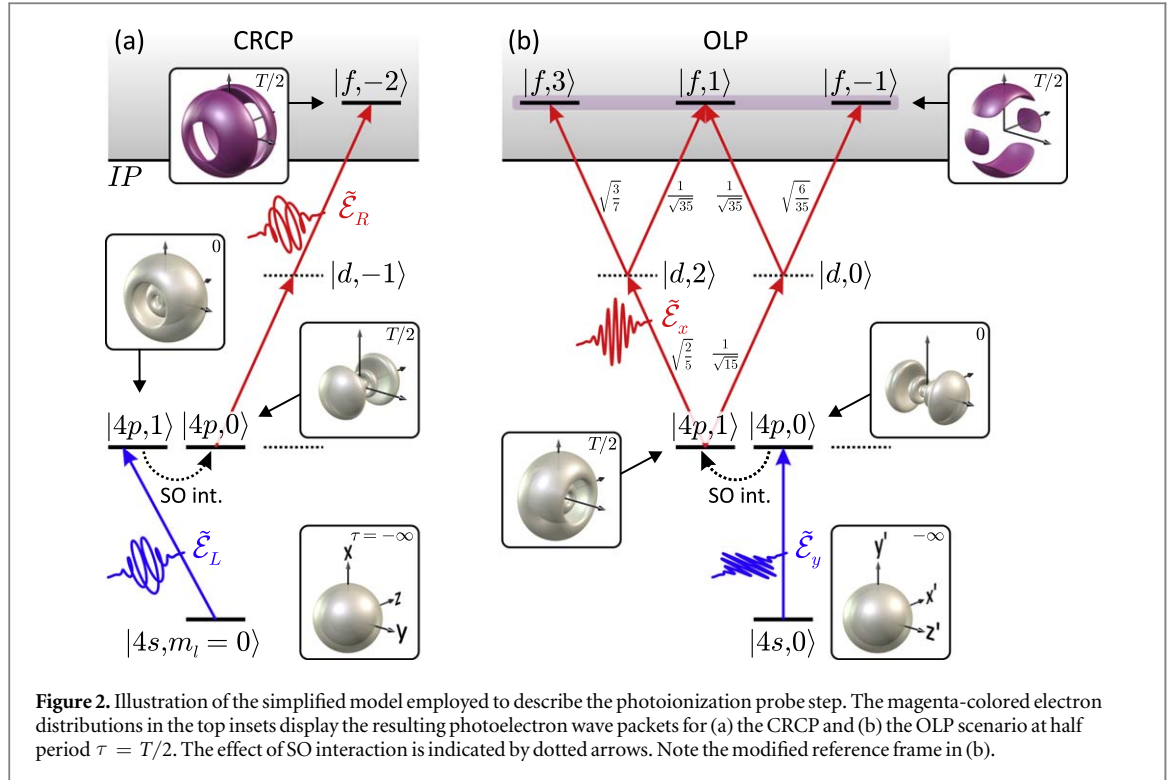
2.2. Photoionization

In the experiment, the SOWP dynamics $\varrho(\boldsymbol{r}, t)$ is mapped into the photoelectron momentum distribution $\mathcal{P}(\varepsilon, \theta, \phi; \tau)$. The two-photon ionization probe step is described using second order time-dependent perturbation theory [20, 39, 40]. Incorporating the electron spin in the treatment increases the number of involved ionization pathways considerably. However, in the numerical simulations presented in sections 4.1 and 4.2, all of these pathways are taken into account. Due to the multitude of contributions, the formalism conceals the basic physical mechanism. To reveal the essential physics of the probe step, we employ a simplified heuristic model based on the description of the ionization process in the uncoupled basis. By considering the spatial part (orbital alignment) of the bound electron wave packet after propagation under SO interaction, we rationalize the angular distribution of the resulting photoelectron wave packet. In the following, we apply the model to the CRCP and the OLP case (see experimental results in sections 4.1 and 4.2) and analyze the photoelectron wave packet created at half period $\tau = \tau_{1/2} = T/2$. For the respective initial states we consider the wave packet $\varrho_{\mathrm{sd}}(\boldsymbol{r}, \tau_{1/2})$ derived in appendices A.2 and A.3 for the spin-down sub-system, as displayed in the top row (middle frame) of figures A1(a) and A2(a), respectively.

2.3. CRCP scenario

The simplified ionization scheme for the CRCP scenario is depicted in figure 2(a). As discussed in appendix A.2, the LCP pump pulse $\tilde{\boldsymbol{\mathcal{E}}}_b$ initially excites the atom into the $|4p, 1\rangle$-state. From here the system evolves under SO interaction and, at half period, reaches a configuration essentially described by the $|4p, 0\rangle$-state (see equation (A.13) and figure A1(a) top row, middle frame). Ionization by the RCP probe pulse $\tilde{\boldsymbol{\mathcal{E}}}_r(\omega) = \tilde{\boldsymbol{\mathcal{E}}}_R(\omega)\boldsymbol{e}_{-1}$ in this time window can therefore be approximated by the single pathway $|4p, 0\rangle \rightarrow |d, -1\rangle \rightarrow |f, -2\rangle$, creating a photoelectron wave packet with $|f, -2\rangle$-type symmetry:

$$\mathcal{P}_{\mathrm{crcp}}(\varepsilon, \theta, \phi; \tau_{1/2}) \propto |R^{(2)}(\varepsilon) Y_{3,-2}(\theta, \phi)|^2. \qquad (2)$$

The radial part $R^{(2)}(\varepsilon)$ describing the photoelectron kinetic energy distribution is determined by the second order optical spectrum of the probe pulse [20, 39] which we assume to be Gaussian-shaped. The corresponding 3D electron density (3D-ED) is illustrated as magenta-colored wave packet in the top inset to figure 2(a). The result predicted by the simplified photoionization model clearly reproduces the experimental result obtained in the CRCP case at $\tau = T/2$ (see figure 5(b)).

Figure 2. Illustration of the simplified model employed to describe the photoionization probe step. The magenta-colored electron distributions in the top insets display the resulting photoelectron wave packets for (a) the CRCP and (b) the OLP scenario at half period $\tau = T/2$. The effect of SO interaction is indicated by dotted arrows. Note the modified reference frame in (b).

2.4. OLP scenario

The simplified ionization scheme for the OLP scenario is depicted in figure 2(b). In this case, we change the reference frame and describe the excitation in a coordinate system with its x'-axis aligned in laser propagation direction and z'-axis defined by the pump pulse polarization (p). The primed coordinate system is indicated in the bottom inset to figure 2(b). The pump pulse is hence given by $\tilde{\boldsymbol{\mathcal{E}}}_b(\omega) = \tilde{\mathcal{E}}_{z'}(\omega)\boldsymbol{e}_{z'}$ and excites the atom via a π-transition into the $|4p, 0\rangle$-state. Subsequently, SO precession guides the system into a state essentially described by the $|4p, 1\rangle$-state (see discussion in appendix A.3 and figure A2(a) top row, middle frame). From here the system is ionized by the s-polarized probe pulse $\tilde{\boldsymbol{\mathcal{E}}}_r(\omega) = \tilde{\mathcal{E}}_{y'}(\omega)\boldsymbol{e}_{y'}$ arriving at half period. In the dipole approximation, the effect of the probe pulse propagating in x'-direction is equivalent to a pulse propagating in z'-direction, since in either case the laser electric field oscillates in y'-direction at the position of the atom. The pulse propagating along the z'-axis, however, may again be decomposed into an LCP and an RCP component driving $\sigma^{\pm}$-transitions in the primed reference frame. As indicated in figure 2(b), this gives rise to four different ionization pathways proceeding via the virtual states $|d, 2\rangle$ and $|d, 0\rangle$ to $|f, 3\rangle$-, $|f, 1\rangle$- and $|f, -1\rangle$-type continua. Evaluation of the relative amplitudes [40] yields the superposition state of the photoelectron wave packet

$$\mathcal{P}_{\text{olp}}(\varepsilon, \theta, \phi; \tau_{1/2}) \propto |R^{(2)}(\varepsilon)|^2 \times \left| Y_{3,3}(\theta, \phi) + \frac{2}{\sqrt{15}}Y_{3,1}(\theta, \phi) + \frac{1}{\sqrt{15}}Y_{3,-1}(\theta, \phi) \right|^2. \tag{3}$$

The corresponding 3D-ED, illustrated as magenta-colored wave packet in the top inset to figure 2(b), is in good qualitative agreement with the experimental and full simulation results obtained in the OLP case at $\tau = T/2$ (see figure 6(b)).

3. Experimental

The two-color pump-probe scheme employed in our experiment combines bichromatic polarization pulse shaping with photoelectron imaging spectroscopy. Retrieval of the 3D photoelectron momentum distribution is achieved by tomographic reconstruction techniques [17]. A sketch of the experimental setup is presented in figure 3.

3.1. Bichromatic polarization shaping

Polarization-shaped bichromatic pump-probe sequences are generated using a shaper-based common-path scheme. A detailed description of the optical setup is given in [20, 41, 42]. Briefly, a home-built 4f polarization pulse shaper equipped with a dual-layer liquid crystal spatial light modulator (LC-SLM; *Jenoptik*, SLM-S640d)

Figure 3. Experimental setup combining bichromatic polarization pulse shaping and photoelectron imaging tomography. See main text for a detailed description. TG: transmission grating, CM: cylindrical mirror, FM: folding mirror, CP: composite polarizer, L: lens, R: repeller, E: extractor, G: ground electrode.
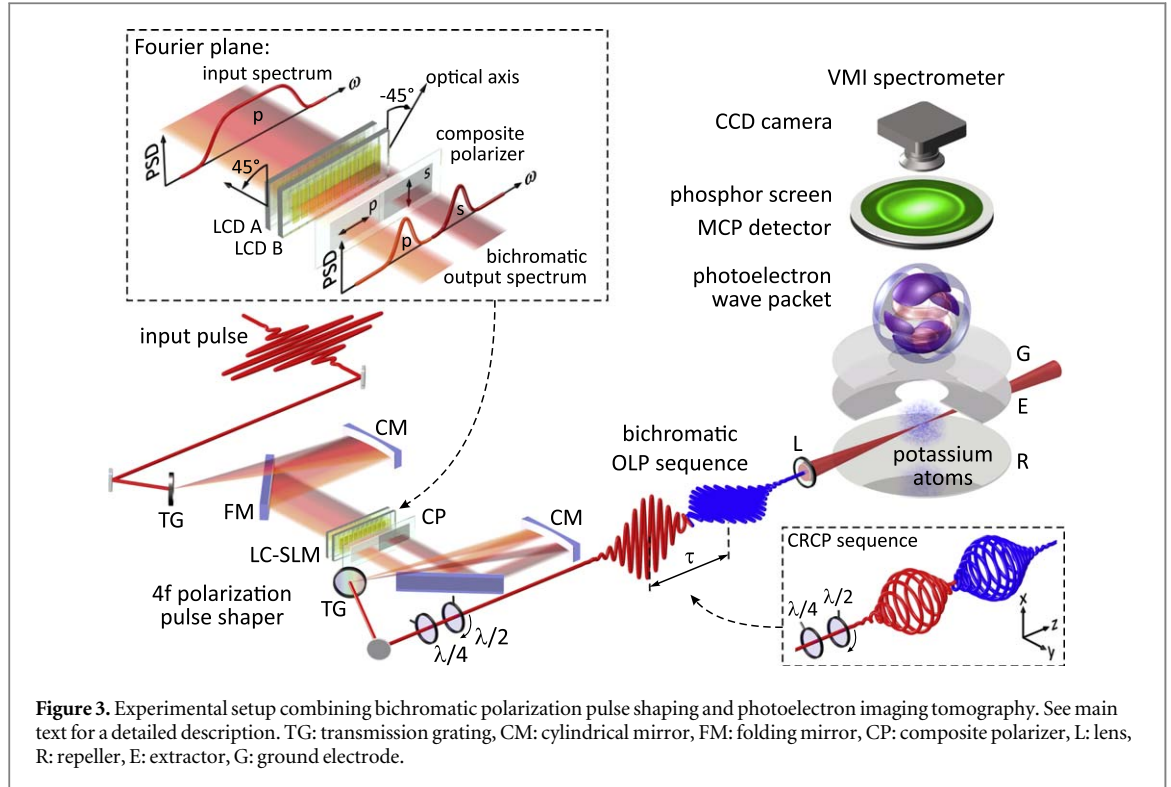
for independent amplitude and phase modulation is employed to sculpture the bichromatic amplitude profile from the spectrum of a 20 fs, 790 nm input pulse provided by an amplified femtosecond laser system (*Femtolasers* Femtopower HR 3 kHz CEP amplifier seeded by a Rainbow 500 oscillator). Using a custom composite polarizer consisting of two adjacent active areas with orthogonal transmission axes (*s*- and *p*-polarized), in the Fourier plane enables independent spectral amplitude and phase modulation of two orthogonally polarized spectral bands (see upper left inset to figure 3). Conversion from OLP to CRCP bichromatic fields is implemented by a superachromatic quarter wave plate at the shaper output with optical axis aligned at $\pm 45°$ with respect to the *x*-axis (see lower right inset to figure 3). The time delay τ between pump and probe pulse is introduced by application of the linear spectral phases
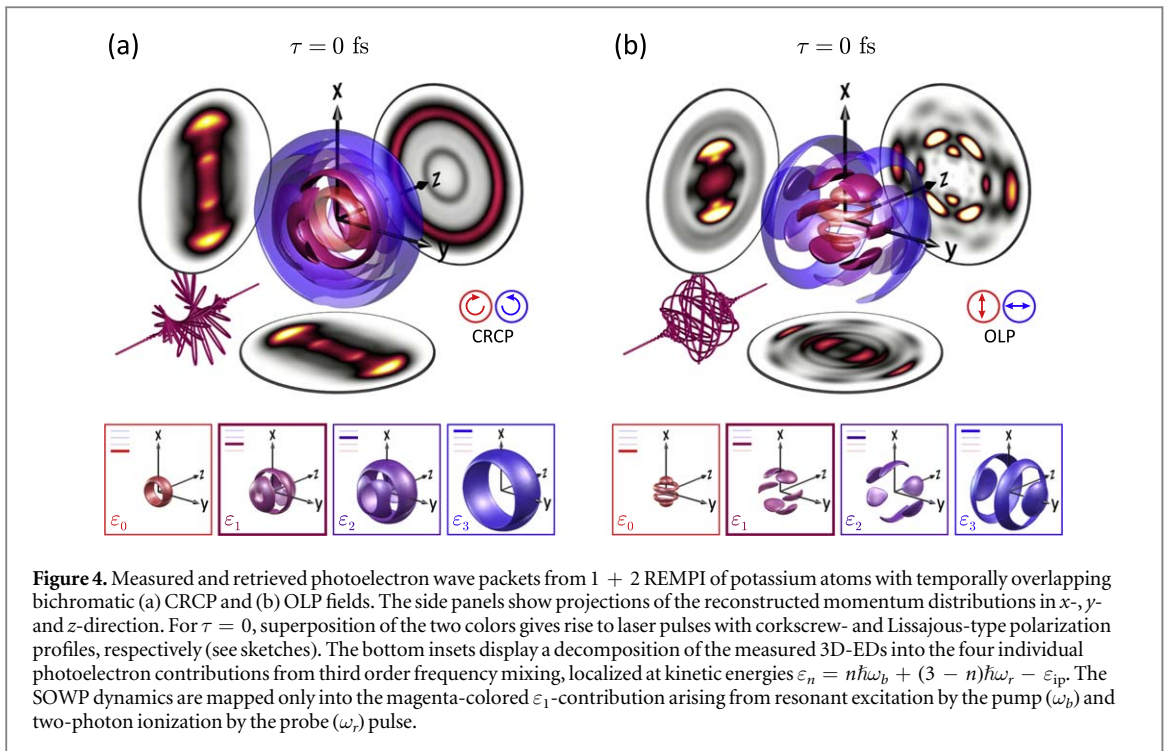
$$\varphi_b(\omega) = -\frac{\tau}{2} \cdot (\omega - \omega_b), \qquad \varphi_r(\omega) = \frac{\tau}{2} \cdot (\omega - \omega_r) \tag{4}$$

to the blue and red band, respectively. From the measured spatial dispersion of 0.25 nm/pixel we estimate a spectral resolution of the pulse shaper of $\Delta\omega \approx 0.75$ mrad fs^{-1}. This corresponds to a shaping window, i.e. maximum applicable time delay of about 8 ps. In addition, the shaper is employed for spectral dispersion management. Residual spectral phases are determined and compensated by adaptive optimization of the second harmonic generation in a β-barium borate crystal using the shaper, the crystal and a spectrometer in a closed loop configuration [41, 43, 44].

3.2. Photoelectron imaging tomography

To study the laser-induced spin dynamics in potassium atoms with 3D spatial resolution, the shaped laser pulses are focused into the interaction region of a VMI spectrometer [14], as shown in figure 3. Potassium vapor (pressure 5×10^{-7} mbar) is provided by an alkali metal dispenser source (*SAES Getters*) mounted parallel to the laser beam (not shown). Photoelectron wave packets from $1 + 2$ resonance-enhanced multiphoton ionization (REMPI) of potassium atoms are imaged onto a multi-channel plate detector in chevron configuration coupled to a phosphor screen (*Scientific Instruments*). The peak intensity in the laser focus of the $f = 250$ mm lens is estimated to be $I_0 \approx 1 \times 10^{11}$ W cm^{-2}. At this intensity, about 2 events per laser shot are detected on the screen [20]. Images of the screen are recorded with a charge-coupled device camera (*Lumenera LW165M*) using an exposure time of 200 ms. Each projection of the 3D-ED was recorded by accumulation of 400 images.

In general, photoionization of atoms with polarization-shaped laser pulses yields 3D-EDs which are not cylindrically symmetric. This precludes a retrieval of the 3D-ED by means of Abel inversion. By employing a tomographic technique [17] for the reconstruction of 3D-EDs from polarization-shaped bichromatic pulses [20], we circumvent symmetry restrictions. The incident laser pulse is rotated about the laser propagation axis (*z*-axis) using a $\lambda/2$ wave plate and various projections of the 3D-ED are recorded for different rotation angles.
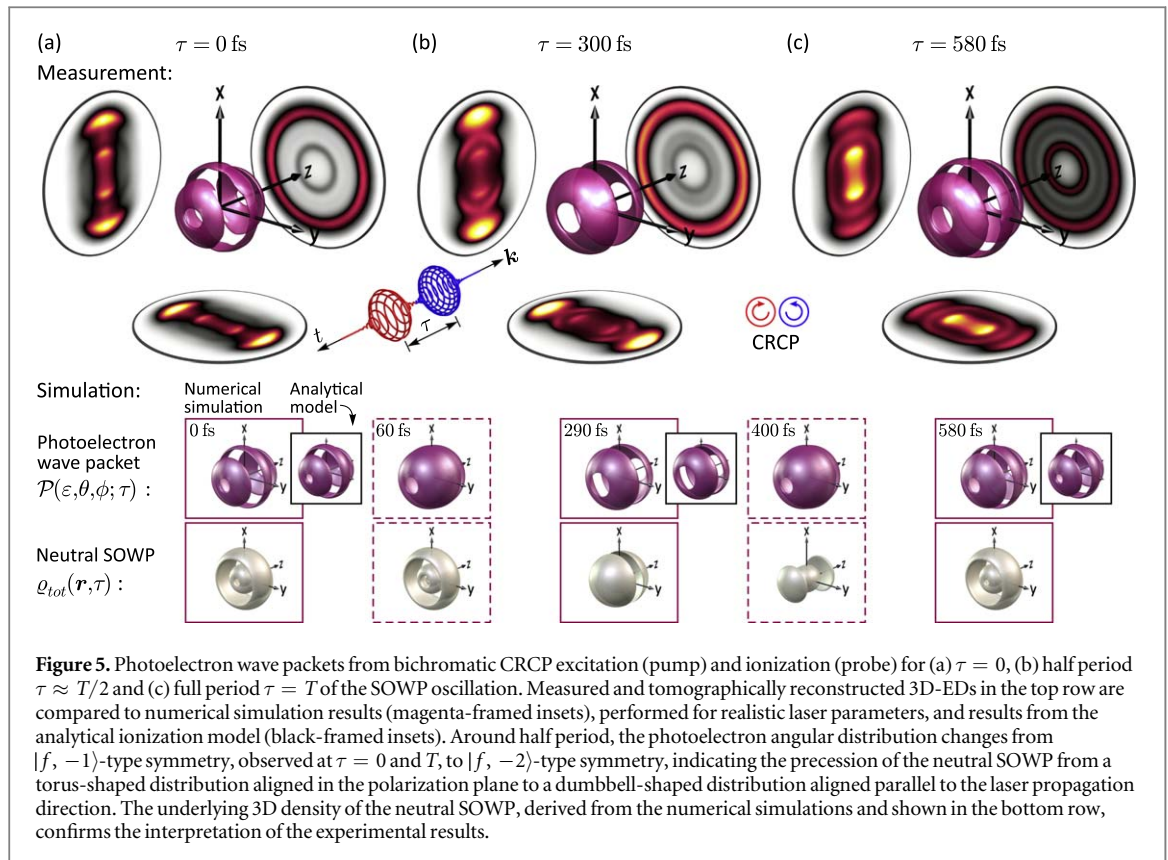
Figure 4. Measured and retrieved photoelectron wave packets from 1 + 2 REMPI of potassium atoms with temporally overlapping bichromatic (a) CRCP and (b) OLP fields. The side panels show projections of the reconstructed momentum distributions in *x*-, *y*- and *z*-direction. For $\tau = 0$, superposition of the two colors gives rise to laser pulses with corkscrew- and Lissajous-type polarization profiles, respectively (see sketches). The bottom insets display a decomposition of the measured 3D-EDs into the four individual photoelectron contributions from third order frequency mixing, localized at kinetic energies $\varepsilon_n = n\hbar\omega_b + (3 - n)\hbar\omega_r - \varepsilon_{ip}$. The SOWP dynamics are mapped only into the magenta-colored ε_1-contribution arising from resonant excitation by the pump (ω_b) and two-photon ionization by the probe (ω_r) pulse.

In the experiments reported here, 45 projections were measured for rotation angles between $-90°$ and $86°$. From the recorded two-dimensional projections, the 3D-EDs are retrieved using the Fourier slice algorithm [21, 45].

4. Results and discussion

In this section, we present the results of two experiments carried out to study the SOWP dynamics induced and probed by shaper-generated bichromatic CRCP and OLP pulse sequences. We start with a brief recapitulation of the experimental results obtained at $\tau = 0$ which have been discussed in more detail in [20]. While the scope of this recent publication was the sculpturing of *static* photoelectron momentum distributions by creation of unusual angular momentum superposition states, the focus of the present study is the observation of ultrafast dynamics by variation of the time delay. Figure 4 shows the tomographically reconstructed and energy-calibrated photoelectron wave packets from CRCP (figure 4(a)) and OLP (figure 4(b)) photoionization at $\tau = 0$. As discussed in section 2.1, four different energy channels ε_n are accessible by three-photon ionization of potassium atoms with bichromatic laser fields. If both pulses overlap in time, photoelectron wave packets from all four channels are observed in different shells of the retrieved 3D-ED. For better visibility, the individual contributions are extracted by application of Gaussian-shaped energy filters, similar to the peeling of an onion, and displayed separately in the bottom insets to figures 4(a) and (b). In the CRCP scenario, we observe the selective creation of angular momentum eigenstates $|f, m_\ell\rangle$ with odd-numbered m_ℓ [20]. In the OLP scenario, we observe rotated $|f, 0\rangle$-type wave packets in the inner- and outermost channel. The outer (inner) contribution is aligned along the *y*-axis (*x*-axis) in accordance with the pump (probe) pulse polarization. In the intermediate channels, two uncommon superposition states are observed, dominated by the interference of the torus-shaped $|f, -3\rangle$- and $|f, 3\rangle$-type wave packets with minor contributions from the $|f, \pm 1\rangle$-states. Because this superposition results in photoelectron wave packets with an approximate six-fold rotational symmetry, we refer to this 3D-ED as 'c_6 wave packet' in the discussion below. In both scenarios, only the magenta-colored wave packet from the ε_1-channel is sensitive to the SOWP dynamics. In the following, we therefore pick the ε_1-contribution and investigate the time evolution of the related 3D-ED by variation of the time delay between the two colors.

4.1. CRCP pump-probe results

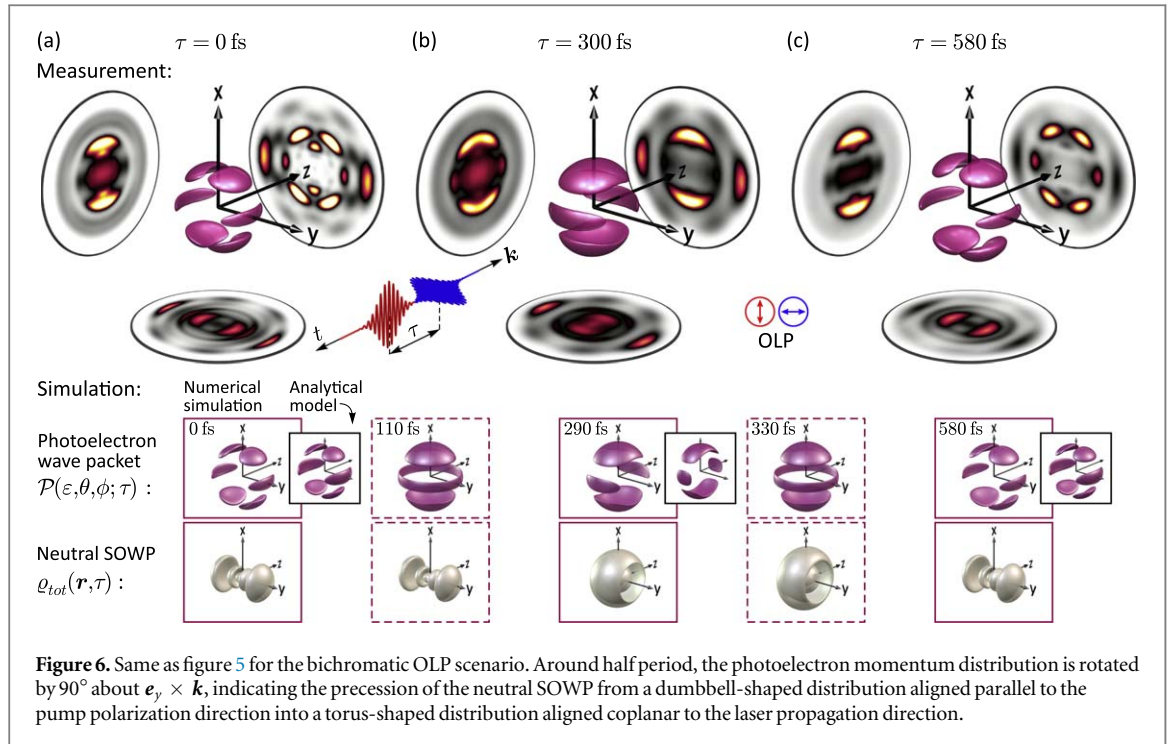The time series of 3D-EDs obtained by 1 + 2 REMPI with time-delayed bichromatic CRCP pulse sequences is presented in figure 5. Three types of data are presented. The top row shows experimental data from the tomographic reconstruction procedure. Below, results from a numerical simulation (magenta-framed insets) are shown along with 3D-EDs predicted by the analytical ionization model (small black-framed insets). The

Figure 5. Photoelectron wave packets from bichromatic CRCP excitation (pump) and ionization (probe) for (a) $\tau = 0$, (b) half period $\tau \approx T/2$ and (c) full period $\tau = T$ of the SOWP oscillation. Measured and tomographically reconstructed 3D-EDs in the top row are compared to numerical simulation results (magenta-framed insets), performed for realistic laser parameters, and results from the analytical ionization model (black-framed insets). Around half period, the photoelectron angular distribution changes from $|f, -1\rangle$-type symmetry, observed at $\tau = 0$ and T, to $|f, -2\rangle$-type symmetry, indicating the precession of the neutral SOWP from a torus-shaped distribution aligned in the polarization plane to a dumbbell-shaped distribution aligned parallel to the laser propagation direction. The underlying 3D density of the neutral SOWP, derived from the numerical simulations and shown in the bottom row, confirms the interpretation of the experimental results.

CRCP sequence consists of a blue LCP pump pulse followed by a red RCP probe pulse separated by a time delay τ. Figure 5(a) shows the 3D-ED from the ε_1-channel (kinetic energies $\varepsilon = 0.25 .. 0.35$ eV) measured at $\tau = 0$ (see figure 4(a)). From the observed $|f, -1\rangle$-type symmetry we infer that the SOWP is initialized in the $|4p, 1\rangle$-state, since the photoelectron wave packet is created by absorption of two σ^- (RCP) photons (see also discussion in appendix A.2). Increasing the time delay to $\tau = 300$ fs, i.e. to roughly half the SOWP oscillation period, yields the 3D-ED shown in figure 5(b). Here, at the turning point of the oscillation, the photoelectron wave packet exhibits distinct $|f, -2\rangle$-symmetry. According to the discussion appendix A.2 and section 2.3, this symmetry indicates that the SOWP has 'precessed' into the $|4p, 0\rangle$-state by SO coupling. Figure 5(c) shows the 3D-ED measured for $\tau = 580$ fs i.e. after a full oscillation period T. Comparison to figure 5(a) confirms that the SOWP has completed one cycle and returned to its origin. Slight differences between the 3D-EDs in (c) and (a), mainly related to the photoelectron yield, are due to the fact, that initially ($\tau = 0$) the red pulse probes the SOWP as it is built up from zero to full amplitude by the pump pulse, whereas at $\tau = T$ the SOWP evolves freely with final amplitude.

The numerical simulations were performed for realistic pulse parameters to supplement the generic analytical description in section 2. The simulations are based on the numerical solution of the time-dependent Schrödinger equation in the coupled basis to calculate the neutral electron dynamics displayed in the bottom frames. Photoionization is described by second order time-dependent perturbation theory, taking all ionization pathways determined by the selection rules $\Delta j = 0, \pm 1$ and $\Delta m_j = \pm 1$ into account. Both spin sub-systems are treated separately. The 3D-ED of each sub-system is derived from the absolute square of the spinor describing the corresponding photoelectron wave packet, similar to the treatment in appendix A.1 (see equations (A.7) and (A.8)).The total 3D-ED, displayed in the top frames, is obtained by summation of the densities from both sub-systems. The simulation results are in excellent agreement with experimental findings and confirm the above analysis of the neutral SOWP dynamics. Moreover, the simulations provide access to any desired stage of the SOWP dynamics. For example we find that the transition between the $|f, -1\rangle$-type 3D-ED at $\tau = 0$ to the $|f, -2\rangle$-type 3D-ED at $\tau = T/2$ takes place around $\tau = 60$ fs. Here the nodal structure of the photoelectron angular distribution changes rapidly and the density becomes almost isotropic (second frame). The transition back to the 3D-ED at $\tau = T$ occurs around $\tau = 400$ fs where the 3D-ED assumes a very similar shape.

In summary, in the case of time-delayed CRCP pulse sequences, we observe a change in the m_ℓ-character of the created photoelectron wave packet induced by SO interaction in the neutral $4p$-state. In particular, the

Figure 6. Same as figure 5 for the bichromatic OLP scenario. Around half period, the photoelectron momentum distribution is rotated by 90° about $e_y \times k$, indicating the precession of the neutral SOWP from a dumbbell-shaped distribution aligned parallel to the pump polarization direction into a torus-shaped distribution aligned coplanar to the laser propagation direction.

observation of an $|f, -2\rangle$-type wave packet completes the set of seven angular momentum eigenstates $|f, m_\ell\rangle$ created by bichromatic REMPI [20] and underscores the power of polarization-tailored bichromatic fields to prepare free electron wave packets in any desired angular momentum state.

4.2. OLP pump-probe results

Although the CRCP pulse sequences discussed in the previous section are not fully symmetric (especially for $\tau \lesssim \Delta t$), the corresponding 3D-EDs turned out to be cylindrically symmetric and could in principle be retrieved by Abel inversion (see figure 5). In contrast, apart from the ε_3-contribution, the 3D-EDs in the OLP case exhibit no cylindrical symmetry suitable for Abel inversion. Therefore, in this case the application of tomographic techniques is essential for the reconstruction of the created photoelectron wave packets. The time series of reconstructed 3D-EDs recorded by 1 + 2 REMPI with a blue *p*-polarized pump followed by a red *s*-polarized probe pulse is illustrated in figure 6. Again we focus on the photoelectron contribution in the ε_1-channel to study the SOWP dynamics. Figure 6(a) shows the c_6 wave packet measured at $\tau = 0$ arising from simultaneous excitation and ionization of the atom via the neutral states $|4p, \pm1\rangle$ [20]. Initially, coherent superposition of these states corresponds to a rotated $|4p, 0\rangle$-state oriented in pump polarization direction (e_y). The associated dumbbell-shaped wave function is discussed in appendix A.3 to describe the initial state of the SOWP from *p*-polarized excitation. While the c_6 wave packet is aligned in the laser polarization plane, the 3D-ED measured around half period $\tau = 300$ fs is rotated by 90° about an axis orthogonal to both the laser polarization and laser propagation direction, i.e. about $e_y \times k$. As shown in figure 6(b), the resulting photoelectron wave packet is aligned in the *x*–*z*-plane normal to e_y and coplanar to k. The top and bottom node in the angular distribution have vanished, reducing the total number of nodes (lobes) from six to four. According to the discussion in section 2.4, this particular shape of the 3D-ED (see figure 2(b)) reflects the evolution of the SOWP from the dumbbell-shaped distribution oriented in *y*-direction into a torus-shaped distribution aligned in the *x*–*z*-plane, thus confirming the analysis in appendix A.3 (see figure A2). 'The wave packet in figure 6(c) is similar to the initial wave packet in (a) indicating the completion of the SOWP oscillation cycle. In analogy to the CRCP case, the 3D-ED at full period exhibits a slightly larger amplitude than at $\tau = 0$.

The numerical simulations shown in the insets are again in very good agreement with the experimental results. In this case, the transitions in the nodal structure occur around $\tau = 110$ fs and 330 fs, respectively. At both instances, the 3D-ED assumes a cylindrically symmetric shape, reminiscent of a rotated $|d, 0\rangle$-state, aligned along the *x*-axis.

In summary, in the case of time-delayed OLP pulse sequences, we observe a counterintuitive rotation of the photoelectron momentum distribution about an axis orthogonal to both the pump polarization vector and the wave vector (*x*-axis). As a result, the photoelectron wave packet created at half period is aligned coplanar to the laser propagation direction.

5. Conclusion and outlook

In this paper, we presented a two-color pump-probe scheme based on the combination of bichromatic polarization pulse shaping and photoelectron imaging tomography. Ultrashort two-color pump-probe pulse sequences with variable states of polarization were generated by amplitude and phase modulation of a femtosecond input pulse using a $4f$ polarization shaper equipped with a custom composite polarizer. Due to the common path geometry of the optical setup, the shaper-based approach benefits from excellent phase stability [46]. Selecting different spectral bands for pump and probe pulse is the key to disentangle the excitation and the interrogation step. The separation of pump and probe signals in the energy-resolved photoelectron spectrum opens an energy window for the background-free detection of the light-induced electron dynamics. The angular resolution provides access to the polar and azimuthal part of the electron wave packet, enabling the observation of angular momentum dynamics.

To exemplify the bichromatic pump-probe technique on a well-established model system, we applied the scheme to time-resolved spatial imaging of ultrafast SOWP dynamics in potassium atoms. We presented the first 3D tomographic reconstruction of photoelectron momentum distributions mapping the coupled angular momentum dynamics in the $4p$ fine structure states. Two different scenarios were investigated utilizing CRCP and OLP bichromatic pulse sequences. Analysis of both scenarios revealed a common underlying neutral dynamics, i.e. the counterintuitive rotation of the SOWP from an initial alignment in the laser polarization plane to an orthogonal alignment parallel or coplanar to the laser propagation direction. In the CRCP case, the orbital realignment manifests in a change in the m_ℓ-character of the measured photoelectron wave packet. In the OLP case, the angular dynamics of the SOWP induces a corresponding rotation of the photoelectron wave packet about $\boldsymbol{e} \times \boldsymbol{k}$. For completeness, corotating circularly polarized (COCP) and parallel linearly polarized (PLP) pump-probe scenarios were also investigated. The physics behind these cases was found to be analogous to the results from the CRCP and the OLP scenario. Similar to the CRCP case, the photoelectron angular dynamics turned out to be cylindrically symmetric, in accordance with the symmetry of the fields, and could be retrieved by Abel inversion. Therefore, the COCP and PLP results are not discussed in this paper. The experiments were supplemented by analytical and numerical models of the spatiotemporal SOWP dynamics and the angular distribution of the created photoelectron wave packets. In particular, we presented an intuitive physical picture of the photoionization dynamics in the presence of SO-interaction. The simulations provided access to the underlying 3D electron dynamics in the neutral atom to confirm the interpretation of the experimental findings and may be used to retrieve the degree of spin polarization of the released photoelectrons.

Our results highlight the power of shaper-generated polarization-shaped bichromatic fields in conjunction with photoelectron tomography for interference-free observation of ultrafast quantum dynamics, opening up new avenues in ultrafast science. For instance, using polarization-*tailored* pump pulses allows to coherently control and image the time evolution of bound electron wave packets in atoms and molecules. Currently, we study the control of SOWPs in the perturbative regime by modulating the spectral phase and amplitude of the pump at the resonance frequencies (see equation (A.4)) as an initial step for the production of highly spin-polarized photoelectron wave packets [11, 30, 32, 33]. In addition, extensions to the strong-field regime for efficient spin-selective production of photoelectrons are investigated.

Promising perspectives arise from the application of the bichromatic polarization shaping scheme to phase-stabilized supercontinua covering the entire visible spectrum [42]. The ultrabroad bandwidth of white light supercontinua permits the generation of waveform-controlled few-cycle pump-probe sequences (down to $\approx$10 fs pulse duration) to investigate even faster electron dynamics in multi-electron systems [29]. The enhanced input bandwidth also supports a larger spectral separation of the two colors (up to 1 eV) to maintain the energetic separation of the photoelectron signals and ensure background-free detection of the dynamics. In addition, shifting the probe pulse to shorter wavelengths may simplify the scheme by realizing a one-photon ionization probe step. Eventually, the available bandwidth allows for an extension of the technique to multi-chromatic polarization-sensitive pump-probe measurements. For example, selecting two bands of commensurable center frequencies enables the creation of bound electron wave packets by M- versus N-photon excitation [47] which are probed by a third color. Such excitations are, in general, sensitive to the absolute phase (CEP) of the bichromatic pump pulse and may be used as spectroscopic tool to extract atomic and molecular properties. A specific application is the design of Rydberg wave packets composed of neutral states with different parity, e.g. by choosing $N = M + 1$, and track the ensuing angular and radial dynamics in real time.

Acknowledgments

Appendix. Theoretical background

In this appendix, we provide a rigorous mathematical description of the spatiotemporal electron dynamics in the potassium 4*p* fine-structure states excited by a resonant polarization-shaped laser pulse, building on the treatment in [11, 24, 25, 33, 35]. We develop an analytical 3D model of the spatial SOWP dynamics (appendix A.1) which is subsequently applied to SOWPs launched by a circularly (appendix A.2) and a linearly polarized (appendix A.3) pump pulse, as used in the experiment.

A.1. Spin–orbit wave packet dynamics

We start with the derivation of an analytical expression for the SOWP wave function and its time evolution after the interaction with the polarization-shaped pump pulse $\tilde{\mathcal{E}}_b(\omega)$, as depicted in figure 1(b). To account for the electron spin, we write the time-dependent excited state wave function as a two component spinor

$$\boldsymbol{\psi}_p(\boldsymbol{r}, t) = \begin{pmatrix} \psi_p^-(\boldsymbol{r}, t) \\ \psi_p^+(\boldsymbol{r}, t) \end{pmatrix}. \tag{A.1}$$

The absolute squares $|\psi_p^-(\boldsymbol{r}, t)|^2$ and $|\psi_p^+(\boldsymbol{r}, t)|^2$ of the spinor components describe the probabilities of finding the electron at time t in the 4*p*-state with spin-down and spin-up, respectively. We define the total 3D density of the SOWP (3D-WP) as

$$\varrho(\boldsymbol{r}, t) = \langle \boldsymbol{\psi}_p | \boldsymbol{\psi}_p \rangle = |\psi_p^-(\boldsymbol{r}, t)|^2 + |\psi_p^+(\boldsymbol{r}, t)|^2, \tag{A.2}$$

which describes the probability of finding the bound electron at time t in the excited 4*p*-state irrespective of its spin [48]. SO coupling is incorporated by describing the atomic system in the coupled basis [16]

$$|\ell, s; j, m_j\rangle = \sum_{m_\ell, m_s} C_{m_\ell\ m_s\ m_j}^{\ell\ \ s\ \ j} |\ell, m_\ell\rangle \otimes |s, m_s\rangle, \tag{A.3}$$

with the Clebsch–Gordon coefficients $C_{m_\ell\ m_s\ m_j}^{\ell\ \ s\ \ j}$. The quantum numbers ℓ, s and j describe the orbital angular momentum, the spin and the total angular momentum of the electron, respectively. The corresponding magnetic quantum numbers are m_ℓ, m_s and m_j. Since $s = 1/2$, we will use the shorthand notation $|\ell_j, m_j\rangle = |\ell, s; j, m_j\rangle$. In the following, we focus on the spin-down sub-system with ground state $|4s_{1/2}, -1/2\rangle$ (see also discussion in section 2.1). However, the treatment of the spin-up sub-system with ground state $|4s_{1/2}, 1/2\rangle$ is fully analogous. Due to the dipole selection rules $\Delta\ell = \pm 1, \Delta j = 0, \pm 1$ and $\Delta m_j = \pm 1$ (see equation (A.5)), the polarization-shaped pump pulse $\mathcal{E}_b(\omega)$ (see equation (1)) couples state $|4s_{1/2}, -1/2\rangle$ to states $|4p_{1/2}, 1/2\rangle$ and $|4p_{3/2}, 1/2\rangle$ by the LCP field component $\tilde{\mathcal{E}}_L(\omega)$ and to state $|4p_{3/2}, -3/2\rangle$ by the RCP field $\tilde{\mathcal{E}}_R(\omega)$, as depicted in figure 1(b). In the weak-field limit, the excited system state at time t after the excitation, i.e. $t \gg \Delta t$, is described by time-dependent perturbation theory as

$$\begin{aligned} |\psi_p(t)\rangle = \frac{i}{\hbar}[&\mu_{21}\tilde{\mathcal{E}}_L(\omega_{1/2})|4p_{1/2}, 1/2\rangle \\ &+ \mu_{31}\tilde{\mathcal{E}}_L(\omega_{3/2})e^{-i\frac{\Delta\varepsilon}{\hbar}t}|4p_{3/2}, 1/2\rangle \\ &+ \mu_{41}\tilde{\mathcal{E}}_R(\omega_{3/2})e^{-i\frac{\Delta\varepsilon}{\hbar}t}|4p_{3/2}, -3/2\rangle]. \end{aligned} \tag{A.4}$$

By replacing the spectral field components $\tilde{\mathcal{E}}_q(\omega_s)$, with $q = L, R$ and $s = 1/2, 3/2$, by the transient spectra $\tilde{\mathcal{E}}_q(t; \omega_s) = \int_{-\infty}^t \mathcal{E}_q(t')e^{i\omega_s t'}dt'$, equation (A.4) is also applicable during the interaction with the pump, i.e. for $t < \Delta t$. For bandwidth-limited resonant and perturbative excitation much shorter than the SOWP period T, as discussed in this paper, the difference is not significant. Therefore, we employed equation (A.4) also for the discussion at $t = 0$ below. The dipole couplings μ_{n1} in equation (A.4) are given by [49]

$$\mu_{n1} \propto (-1)^{\frac{1}{2} - m_{j,n}}\sqrt{2j_n + 1} \begin{Bmatrix} 1 & j_n & \frac{1}{2} \\ \frac{1}{2} & 0 & 1 \end{Bmatrix} \begin{pmatrix} \frac{1}{2} & 1 & j_n \\ m_{j,1} & \Delta m_{j,n} & -m_{j,n} \end{pmatrix} \tag{A.5}$$

with $m_{j,1} = -1/2$ for the spin-down sub-system and $\Delta m_{j,n} = m_{j,n} - m_{j,1}$. The index $n = 2, 3, 4$ labels the three excited states $|4p_{j_n}, m_{j,n}\rangle$. The expressions in parentheses and curly brackets are the Wigner 3*j*- and 6*j*-symbols, respectively. To obtain the two spinor components $\psi_p^\pm(\boldsymbol{r}, t)$ in equation (A.1), the state vector $|\psi_p(t)\rangle$ is transformed to the uncoupled basis and decomposed into a spin-down and a spin-up component

$$|\psi_p(t)\rangle = |\psi_p^-(t)\rangle \otimes |\Downarrow\rangle + |\psi_p^+(t)\rangle \otimes |\Uparrow\rangle. \tag{A.6}$$

To this end, we insert equation (A.3) into equation (A.4) and sort the different terms by spin orientation. Making use of equation (A.5) to evaluate the dipole couplings, we find for the spin-down component

$$|\psi_p^-(t)\rangle \propto -[2\tilde{\mathcal{E}}_L(\omega_{1/2}) + \tilde{\mathcal{E}}_L(\omega_{3/2})e^{-i\frac{\Delta\varepsilon}{\hbar}t}]|4p, 1\rangle$$
$$- 3\tilde{\mathcal{E}}_R(\omega_{3/2})e^{-i\frac{\Delta\varepsilon}{\hbar}t}|4p, -1\rangle \tag{A.7}$$

and for the spin-up component

$$|\psi_p^+(t)\rangle \propto \sqrt{2}\,[\tilde{\mathcal{E}}_L(\omega_{1/2}) - \tilde{\mathcal{E}}_L(\omega_{3/2})e^{-i\frac{\Delta\varepsilon}{\hbar}t}]|4p, 0\rangle. \tag{A.8}$$

In both expressions, a global factor of $(3\sqrt{6})^{-1}$ was suppressed for better readability. Analogously, we obtain for the spinor components of the spin-up subsystem the expressions

$$|\psi_p^-(t)\rangle \propto \sqrt{2}\,[\tilde{\mathcal{E}}_R(\omega_{1/2}) - \tilde{\mathcal{E}}_R(\omega_{3/2})e^{-i\frac{\Delta\varepsilon}{\hbar}t}]|4p, 0\rangle \tag{A.9}$$

and

$$|\psi_p^+(t)\rangle \propto -[2\tilde{\mathcal{E}}_R(\omega_{1/2}) + \tilde{\mathcal{E}}_R(\omega_{3/2})e^{-i\frac{\Delta\varepsilon}{\hbar}t}]|4p, -1\rangle - 3\tilde{\mathcal{E}}_L(\omega_{3/2})e^{-i\frac{\Delta\varepsilon}{\hbar}t}|4p, 1\rangle. \tag{A.10}$$

In the following, equations (A.7)–(A.10) are analyzed for two prototypical pump pulse polarization states. First, we discuss the SOWP dynamics induced by a circularly polarized pump pulse. Subsequently, we discuss the linearly polarized case.

A.2. Circularly polarized pump

We start with the discussion of the CRCP scenario in the spin-down sub-system. Without loss of generality, we consider an LCP pump, i.e. $\tilde{\mathcal{E}}_R(\omega) \equiv 0$ and $\tilde{\boldsymbol{\mathcal{E}}}_b(\omega) = \tilde{\mathcal{E}}_L(\omega)\boldsymbol{e}_1$. Since the spectral bandwidth of the pulse is much larger than the fine structure splitting, we assume that $\tilde{\mathcal{E}}_L(\omega_{1/2}) \approx \tilde{\mathcal{E}}_L(\omega_{3/2})$. In this case, equations (A.7) and (A.8) simplify to

$$|\psi_p^-(t)\rangle \propto -(2 + e^{-i\frac{\Delta\varepsilon}{\hbar}t})|4p, 1\rangle, \tag{A.11}$$

$$|\psi_p^+(t)\rangle \propto \sqrt{2}\,(1 - e^{-i\frac{\Delta\varepsilon}{\hbar}t})|4p, 0\rangle. \tag{A.12}$$
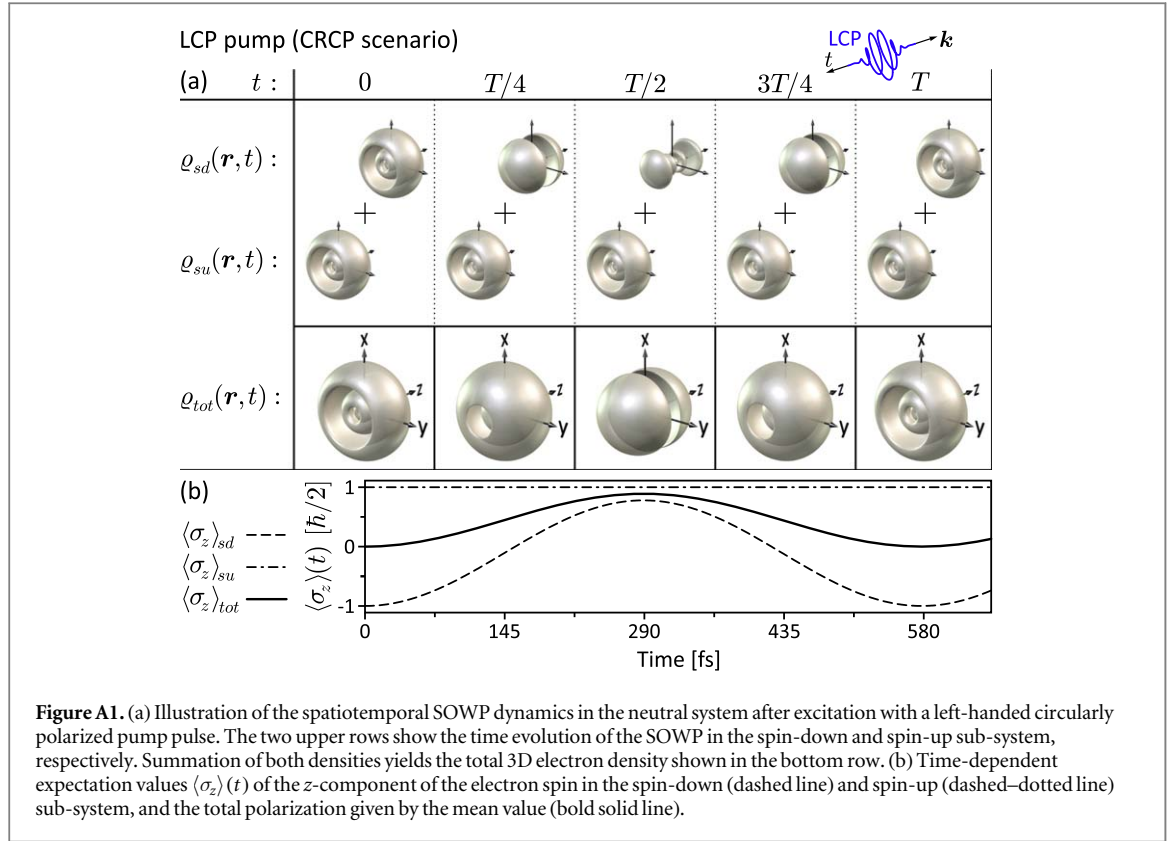
According to equation (A.12), the spin-up component has $|4p, 0\rangle$-character. The related wave function is $\psi_p^+(\boldsymbol{r}, t) = \langle\boldsymbol{r}|\psi_p^+(t)\rangle \propto R_{4p}(r)Y_{1,0}(\theta, \phi)$, where $R_{4p}(r)$ denotes the radial part and the spherical harmonic $Y_{1,0}(\theta, \phi)$ describes the angular part. The corresponding probability density is a dumbbell-shaped orbital aligned along the laser propagation direction ($\boldsymbol{k}$, z-axis) which is displayed in the inset (ii) (top row) to figure 1(b). At first glance, the emergence of this contribution is unexpected for two reasons. First, excitation of the $|\psi_p^+(t)\rangle$ state from the spin-down ground state corresponds to an apparent spin-flip, which would not be induced optically by interaction with the laser electric field. Second, the excited state wave function resulting from laser excitation is generally aligned in the laser polarization plane (x–y-plane) rather than in propagation direction. Indeed, inspection of equation (A.12) shows that at $t = 0$ the amplitude of state $|\psi_p^+(t)\rangle$ vanishes due to destructive interference of the two spin-up contributions associated with the excited states $|4p_{1/2}, 1/2\rangle$ and $|4p_{3/2}, 1/2\rangle$ (see figure 1(b)), confirming the above reasoning.

The spin-down component in equation (A.11) is characterized by the $|4p, 1\rangle$ state. The related spinor component $\psi_p^-(\boldsymbol{r}, t) = \langle\boldsymbol{r}|\psi_p^-(t)\rangle \propto R_{4p}(r)Y_{1,1}(\theta, \phi)$ corresponds to a torus aligned in the laser polarization plane, as displayed in the inset (ii) (bottom row) to figure 1(b). In accordance with LCP excitation of the $4s \to 4p$ transition, this torus-shaped orbital determines the initial shape of the 3D-WP $\varrho_{sd}(\boldsymbol{r}, t = 0)$ in the spin-down sub-system completely (see figure A1(a), top row, first frame).

The above findings hold for $t = 0$ as well as for any integer multiple of the SOWP oscillation period $\tau_n = nT = nh/\Delta\varepsilon$. Intermediately, the system evolves under SO interaction which, in a semi-classical picture, induces a precession of the spin and orbital angular momentum about the total angular momentum [25]. In a quantum mechanical framework, this precession is expressed by the time-dependent amplitude variation of both spin components in equations (A.11) and (A.12). In particular, the two spin-up contributions in equation (A.12) gradually shift in-phase due to their eigenenergy difference of $\Delta\varepsilon$. Constructive interference of both contributions occurs at half period $\tau_{1/2} = T/2$, where the exponential function in equation (A.12) is $e^{-i\frac{\Delta\varepsilon}{\hbar}\tau_{1/2}} = -1$. At this instant, the amplitude of the spin-up component $|\psi_p^+(\tau_{1/2})\rangle$ is maximized while the spin-down component $|\psi_p^-(\tau_{1/2})\rangle$ is minimized. As a result, the electron state has evolved from strictly spin-down ($t = 0$) into a coherent superposition of both spin species. The complete time-evolution of the 3D-WP $\varrho_{sd}(\boldsymbol{r}, t)$ in the spin-down sub-system during the first oscillation period is illustrated in the top row of figure A1(a). For $t = T/2$ we find the expression

$$\varrho_{sd}(\boldsymbol{r}, \tau_{1/2}) \propto R_{4p}^2(r)[|Y_{1,1}(\theta, \phi)|^2 + 8\,|Y_{1,0}(\theta, \phi)|^2], \tag{A.13}$$

implying that at half period the 3D-WP is even dominated by the spin-up contribution described by the $Y_{1,0}(\theta, \phi)$-term. Therefore, the shape of the SOWP is characterized by a dumbbell aligned along the laser propagation direction, as shown in the upper row and middle frame of figure A1(a). The probability ratio of the two spin orientations is $P_-(\tau_{1/2}):P_+(\tau_{1/2}) = 1:8$, i.e. after circularly polarized excitation of the spin-down sub-

Figure A1. (a) Illustration of the spatiotemporal SOWP dynamics in the neutral system after excitation with a left-handed circularly polarized pump pulse. The two upper rows show the time evolution of the SOWP in the spin-down and spin-up sub-system, respectively. Summation of both densities yields the total 3D electron density shown in the bottom row. (b) Time-dependent expectation values $\langle \sigma_z \rangle (t)$ of the z-component of the electron spin in the spin-down (dashed line) and spin-up (dashed–dotted line) sub-system, and the total polarization given by the mean value (bold solid line).

system the probability of finding the excited electron at time $\tau_{1/2}$ with its spin flipped is $P_+ (\tau_{1/2}) = 88.9\%$ [24, 33].

The ultrafast spin dynamics is also captured by the expectation value (in units of $\hbar/2$)

$$\langle \sigma_z \rangle (t) = \langle \boldsymbol{\psi}_p(t) | \sigma_z | \boldsymbol{\psi}_p(t) \rangle = P_-(t) \cdot (-1) + P_+(t) \cdot 1, \tag{A.14}$$

where σ_z is the Pauli matrix related to the z-component of the electron spin. The expectation value $\langle \sigma_z \rangle_{sd} (t)$ for the spin-down sub-system, shown as a dashed line in figure A1(b), evolves from its initial value $\langle \sigma_z \rangle_{sd} (0) = -1$ to $\langle \sigma_z \rangle_{sd} (\tau_{1/2}) = P_+(\tau_{1/2}) - P_-(\tau_{1/2}) = 7/9$ at half period, indicating the approximate spin-flip. The expectation values of the x- and y-component vanish exactly, $\langle \sigma_x \rangle_{sd} (t) = \langle \sigma_y \rangle_{sd} (t) \equiv 0$.

An analogous treatment of the spin-up sub-system reveals, that here the LCP pump pulse excites only the $|4p_{3/2}, 3/2\rangle$-state composed exclusively of the spin-up component:

$$|\psi_p^-(t)\rangle = 0, \tag{A.15}$$

$$|\psi_p^+(t)\rangle \propto -3 e^{-i\frac{\Delta\varepsilon}{\hbar}t} |4p, 1\rangle. \tag{A.16}$$

Consequently, the corresponding 3D-WP is time-independent

$$\varrho_{su}(\boldsymbol{r}, t) \propto 9 R_{4p}^2(r) |Y_{1,1}(\theta, \phi)|^2, \tag{A.17}$$

as illustrated in the middle row of figure A1(a), and the expectation value for the z-component of the spin is constant, $\langle \sigma_z \rangle_{su} (t) \equiv 1$ (dashed–dotted line in figure A1(b)) Therefore, LCP excitation of an unpolarized ensemble of atoms will result in a net spin-up polarization of 94.4% at half period, as expressed by the bold solid line in figure A1(b). The time evolution of the *total* 3D-density $\varrho_{tot}(\boldsymbol{r}, t) = \varrho_{sd}(\boldsymbol{r}, t) + \varrho_{su}(\boldsymbol{r}, t)$ is presented in the bottom row of figure A1(a). Under SO interaction, the total 3D-WP evolves from a torus-type p-orbital aligned in the polarization plane at $t = 0$ into a dumbbell-shaped distribution oriented along the laser propagation direction at $t = T/2$ (middle frame) and back.

A.3. Linearly polarized pump
In the OLP scenario, we consider a horizontally (p) polarized pump, i.e. $\tilde{\boldsymbol{\mathcal{E}}}_b(\omega) = \tilde{\mathcal{E}}_y(\omega) \boldsymbol{e}_y$. In the spherical basis, linear polarization along the y-direction is described by a superposition of the two circularly polarized fields
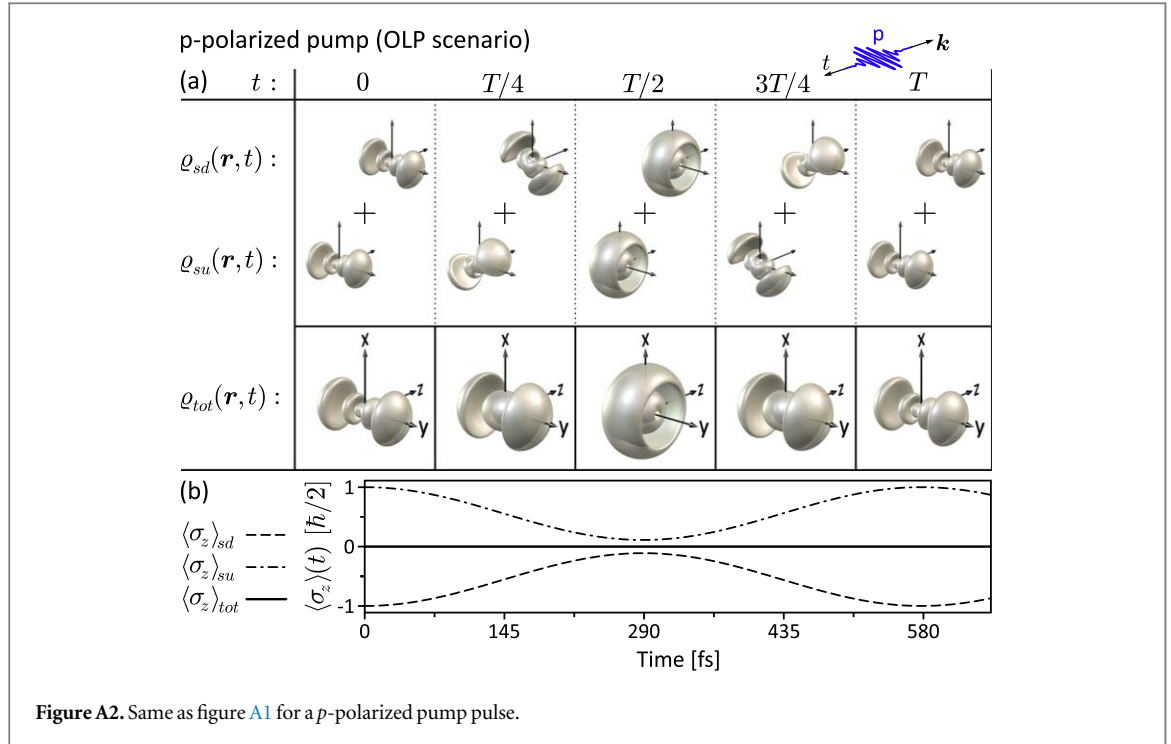
Figure A2. Same as figure A1 for a *p*-polarized pump pulse.

$\tilde{\mathcal{E}}_L(\omega) = \tilde{\mathcal{E}}_R(\omega) = \tilde{\mathcal{E}}_y(\omega)/\sqrt{2}$ with the same shape and amplitude. Assuming that $\tilde{\mathcal{E}}_y(\omega_{1/2}) \approx \tilde{\mathcal{E}}_y(\omega_{3/2})$, equations (A.7) and (A.8) reduce to

$$|\psi_p^-(t)\rangle \propto -(2 + e^{-i\frac{\Delta\varepsilon}{\hbar}t})|4p, 1\rangle - 3e^{-i\frac{\Delta\varepsilon}{\hbar}t}|4p, -1\rangle \tag{A.18}$$

$$|\psi_p^+(t)\rangle \propto \sqrt{2}(1 - e^{-i\frac{\Delta\varepsilon}{\hbar}t})|4p, 0\rangle. \tag{A.19}$$

The spin-up component in equation (A.19) is identical to the CRCP case (see equation (A.12)), because the spin-up contributions are addressed *exclusively* by the LCP field. Hence, $\psi_p^+(\boldsymbol{r}, t)$ vanishes initially ($t = 0$) due to destructive interference of the two spin-up contributions. The spin-down component in equation (A.18) exhibits an additional term proportional to state $|4p, -1\rangle$ excited by the RCP field. Therefore, the related spinor component $\psi_p^-(\boldsymbol{r}, 0)$ is a coherent superposition of two counterrotating torus-shaped wave functions, both of which are aligned in the laser polarization plane. For $t = 0$ the spin-down wave function reads $\psi_p^-(\boldsymbol{r}, 0) \propto R_{4p}(r)[Y_{1,1}(\theta, \phi) - Y_{1,-1}(\theta, \phi)]$, which corresponds to a dumbbell-shaped orbital aligned along the laser polarization direction (*y*-axis; see figure A2(a), top row, first frame). In accordance with *p*-polarized excitation of the $4s \rightarrow 4p$ transition, this orbital solely determines the initial shape of the 3D-WP $\varrho_{sd}(\boldsymbol{r}, 0)$ in the spin-down sub-system.

The complete time evolution of $\varrho_{sd}(\boldsymbol{r}, t)$ is illustrated in the top row of figure A2(a). Under SO interaction, the 3D-WP starts to rotate in positive ϕ-direction and simultaneously morphs into a torus-shaped orbital aligned parallel to the *x*–*z*-plane (middle frame) at half period. The corresponding density reads

$$\varrho_{sd}(\boldsymbol{r}, \tau_{1/2}) \propto R_{4p}^2(r)[|Y_{1,1}(\theta, \phi) + 3Y_{1,-1}(\theta, \phi)|^2 + 8\,|Y_{1,0}(\theta, \phi)|^2], \tag{A.20}$$

which describes a superposition of spin-down and spin-up with a probability ratio of $P_-\,(\tau_{1/2}){:}P_+\,(\tau_{1/2}) = 5{:}4$. In this case, the probability of finding the excited electron at time $\tau_{1/2}$ with its spin flipped is only $P_+\,(\tau_{1/2}) = 44.4\%$. Accordingly, the corresponding expectation value $\langle\sigma_z\rangle_{sd}(t)$ displayed in figure A2(b) (dashed line) reaches a maximum of $\langle\sigma_z\rangle_{sd}(\tau_{1/2}) = -1/9$.

Similar dynamics are obtained in the spin-up sub-system. Here the two spinor components are given by

$$|\psi_p^-(t)\rangle \propto \sqrt{2}(1 - e^{-i\frac{\Delta\varepsilon}{\hbar}t})|4p, 0\rangle, \tag{A.21}$$

$$|\psi_p^+(t)\rangle \propto -(2 + e^{-i\frac{\Delta\varepsilon}{\hbar}t})|4p, -1\rangle - 3e^{-i\frac{\Delta\varepsilon}{\hbar}t}|4p, 1\rangle. \tag{A.22}$$

Apparently, states $|4p, 1\rangle$ and $|4p, -1\rangle$ exchange their roles in comparison to the spin-down sub-system (see equations (A.18) and (A.19)). As a consequence, the 3D-WP $\varrho_{su}(\boldsymbol{r}, t)$ undergoes the same time evolution only with reversed angular (ϕ) dynamics. This is illustrated in the middle row of figure A2(a). At half period, the 3D-WP has evolved into the same torus-shaped orbital aligned in the *x*–*z*-plane which, in this case, takes the form

$$\varrho_{su}(\boldsymbol{r}, \tau_{1/2}) \propto R_{4p}^2(r)[|Y_{1,-1}(\theta, \phi) + 3\,Y_{1,1}(\theta, \phi)|^2 + 8\,|Y_{1,0}(\theta, \phi)|^2]. \tag{A.23}$$

The equivalence between this expression and equation (A.20) is revealed by invoking the symmetry relation $Y_{l,-m}(\theta, \phi) = (-1)^m Y_{l,m}^*(\theta, \phi)$. The corresponding spin precession, described by the expectation value $\langle \sigma_z \rangle_{\mathrm{su}}(t)$ in figure A2(b) (dashed–dotted line), is also inverted compared to the spin-down sub-system. Starting from $\langle \sigma_z \rangle_{\mathrm{su}}(0) = 1$, the expectation value reaches a minimum of $\langle \sigma_z \rangle_{\mathrm{su}}(\tau_{1/2}) = 1/9$ at half period. Due to this mirror symmetry of the spin dynamics in both sub-systems, no net polarization is induced in an isotropic ensemble of atoms by linearly polarized excitation (bold solid line in figure A2(b)). The total 3D-density $\varrho_{\mathrm{tot}}(\boldsymbol{r}, t)$, presented in the bottom row of figure A2(a), evolves from a p-type dumbbell oriented in laser polarization direction at $t = 0$ into a torus aligned orthogonal to the polarization at the turning point $t = T/2$ and back.

References

[1] Zewail A H 2000 Femtochemistry: atomic-scale dynamics of the chemical bond *J. Phys. Chem.* **104** 5660–94

[2] Manz J and Woeste L 1995 *Femtosecond Chemistry* (Weinheim: VCH)

[3] Stolow A, Bragg A E and Neumark D M 2004 Femtosecond time-resolved photoelectron spectroscopy *Chem. Rev.* **104** 1719–57

[4] Corkum P B and Krausz F 2007 Attosecond science *Nat. Phys.* **3** 381–7

[5] Kling M F and Vrakking M J J 2008 Attosecond electron dynamics *Annu. Rev. Phys. Chem.* **59** 463–99

[6] Pfeifer T, Abel M J, Nagel P M, Jullien A, Loh Z H, Bell J, Neumark D M and Leone S R 2008 Time-resolved spectroscopy of attosecond quantum dynamics *Chem. Phys. Lett.* **463** 11–24

[7] Krausz F and Ivanov M 2009 Attosecond physics *Rev. Mod. Phys.* **81** 163–234

[8] Gallmann Lukas, Cirelli Claudio and Keller Ursula 2012 Attosecond science: recent highlights and future trends *Annu. Rev. Phys. Chem.* **63** 447–69

[9] Calegari F, Sansone G, Stagira S, Vozzi C and Nisoli M 2016 Advances in attosecond science *J. Phys. B: At. Mol. Opt. Phys.* **49** 062001

[10] Brixner T, Krampert G, Pfeifer T, Selle R, Gerber G, Wollenhaupt M, Graefe O, Horn C, Liese D and Baumert T 2004 Quantum control by ultrafast polarization shaping *Phys. Rev. Lett.* **92** 208301

[11] Sokell E, Zamith S, Bouchene M A and Girard B 2000 Polarization-dependent pump-probe studies in atomic fine-structure levels: towards the production of spin-polarized electrons *J. Phys. B: At. Mol. Opt. Phys.* **33** 2005–15

[12] Assion A, Geisler M, Helbing J, Seyfried V and Baumert T 1996 Femtosecond pump-probe photoelectron spectroscopy: mapping of vibrational wave-packet motion *Phys. Rev.* A **54** 4605–8

[13] Frohnmeyer T, Hofmann M, Strehle M and Baumert T 1999 Mapping molecular dynamics (na 2) in intense laser fields: another dimension to femtochemistry *Chem. Phys. Lett.* **312** 447–54

[14] Eppink A T J B and Parker D H 1997 Velocity map imaging of ions and electrons using electrostatic lenses: application in photoelectron and photofragment ion imaging of molecular oxygen *Rev. Sci. Instrum.* **68** 3477–84

[15] Dörner R, Mergel V, Jagutzki O, Spielberger L, Ullrich J, Moshammer R and Schmidt-Böcking H 2000 Cold target recoil ion momentum spectroscopy: a 'momentum microscope' to view atomic collision dynamics *Phys. Rep.* **330** 95–192

[16] Zare R N 2007 *Angular Momentum: Understanding Spatial Aspects in Chemistry and Physics* (New York: Dover)

[17] Wollenhaupt M, Krug M, Köhler J, Bayer T, Sarpe-Tudoran C and Baumert T 2009 Three-dimensional tomographic reconstruction of ultrashort free electron wave packets *Appl. Phys.* B **95** 647–51

[18] Wollenhaupt M, Lux C, Krug M and Baumert T 2013 Tomographic reconstruction of designer free-electron wave packets *Chem. Phys. Chem.* **14** 1341–9

[19] Pengel D, Kerbstadt S, Johannmeyer D, Englert L, Bayer T and Wollenhaupt M 2017 Electron vortices in femtosecond multiphoton ionization *Phys. Rev. Lett.* **118** 053003

[20] Kerbstadt S, Pengel D, Johannmeyer D, Englert L, Bayer T and Wollenhaupt M 2017 Control of photoelectron momentum distributions by bichromatic polarization-shaped laser fields *New J. Phys.* **19** 103017

[21] Pengel D, Kerbstadt S, Englert L, Bayer T and Wollenhaupt M 2017 Control of three-dimensional electron vortices from femtosecond multiphoton ionization *Phys. Rev.* A **96** 043426

[22] Christian J F, Snoek L C, Clement S G and van der Zande W J 1996 Application of associative ionization to the observation of quantum beats in low-lying atomic resonances *Phys. Rev.* A **53** 1894–9

[23] Ramswell J A, Stavros V G, Lei J, Hong Q and Fielding H H 1999 Observation of autoionizing Rydberg-electron wave packets in xe *Phys. Rev.* A **59** 2186–9

[24] Wen H, Pisharody S N, Murray J M and Bucksbaum P H 2006 Observing angular precession of a Rydberg wave packet due to spin–orbit coupling by orthogonally polarized weak half-cycle pulses *Phys. Rev.* A **73** 052504

[25] Zamith S, Bouchene M A, Sokell E, Nicole C, Blanchet V and Girard B 2000 Observation of the oscillation of an angular wavepacket *Eur. Phys. J.* D **12** 255–61

[26] Gilb S, Torres E A and Leone S R 2006 Mapping of time-dependent electron orbital alignment *J. Phys. B: At. Mol. Opt. Phys.* **39** 4231

[27] Doughty B, Haber L H, Hackett C and Leone S R 2011 Photoelectron angular distributions from autoionizing 4s(1)4p(6)6p(1) states in atomic krypton probed with femtosecond time resolution *J. Chem. Phys.* **134** 094307

[28] Plenge J, Wirsing A, Raschpichler C, Wassermann B and Rühl E 2011 Control of coherent excitation of neon in the extreme ultraviolet regime *Faraday Discuss.* **153** 361–73

[29] Goulielmakis E *et al* 2010 Real-time observation of valence electron motion *Nature* **466** 739–43

[30] Chatel B, Bigourd D, Weber S and Girard B 2008 Coherent control of spin–orbit precession with shaped laser pulses *J. Phys. B: At. Mol. Opt. Phys.* **41** 074023

[31] Zhdanovich S, Hepburn J W and Milner V 2011 Strong-field effects in rabi oscillations between a single state and a superposition of states *Phys. Rev.* A **84** 063405

[32] Braun H, Bayer T, Pengel D, Wollenhaupt M and Baumert T 2017 Simultaneous observation of transient and final state dynamics in ultrafast strong-field excitation via time-resolved photoelectron spectroscopy *J. Mod. Opt.* **64** 1042–53

[33] Bouchene M A, Zamith S and Girard B 2001 Spin-polarized electrons produced by a sequence of two femtosecond pulses. Calculation of differential and global polarization rates *J. Phys. B: At. Mol. Opt. Phys.* **34** 1497–512

[34] Nakajima T 2004 Control of the spin polarization of photoelectrons/photoions using short laser pulses *Appl. Phys. Lett.* **84** 3786–8

[35] Nicole C, Bouchene M A, Zamith S, Melikechi N and Girard B 1999 Saturation of wave-packet interferences: direct observation of spin precession in potassium atoms *Phys. Rev.* A **60** R1755–8

[36] Bethe H A and Salpeter E E 1957 *Quantum Mechanics of One- and Two-Electron Atoms* (Berlin: Springer)

[37] Fano U 1985 Propensity rules—an analytical approach *Phys. Rev. A* **32** 617

[38] Hockett P, Wollenhaupt M, Lux C and Baumert T 2014 Complete photoionization experiments via ultra-fast coherent control with polarization-multiplexing *Phys. Rev. Lett.* **112** 223001

[39] Meshulach D and Silberberg Y 1999 Coherent quantum control of multiphoton transitions by shaped ultrashort optical pulses *Phys. Rev. A* **60** 1287–92

[40] Wollenhaupt M, Krug M, Köhler J, Bayer T, Sarpe-Tudoran C and Baumert T 2009 Photoelectron angular distributions from strong-field coherent electronic excitation *Appl. Phys. B* **95** 245–59

[41] Kerbstadt S, Englert L, Bayer T and Wollenhaupt M 2017 Ultrashort polarization-tailored bichromatic fields *J. Mod. Opt.* **64** 1010

[42] Kerbstadt S, Timmer D, Englert L, Bayer T and Wollenhaupt M 2017 Ultrashort polarization-tailored bichromatic fields from a cep-stable white light supercontinuum *Opt. Express* **25** 12518

[43] Baumert T, Brixner T, Seyfried V, Strehle M and Gerber G 1997 Femtosecond pulse shaping by an evolutionary algorithm with feedback *Appl. Phys. B* **65** 779–82

[44] Yelin D, Meshulach D and Silberberg Y 1997 Adaptive femtosecond pulse compression *Opt. Lett.* **22** 1793–5

[45] Kak A C and Slaney M 1988 *Principles of Computerized Tomographic Imaging* (New York: IEEE)

[46] Köhler J, Wollenhaupt M, Bayer T, Sarpe C and Baumert T 2011 Zeptosecond precision pulse shaping *Opt. Express* **19** 11638–53

[47] Kerbstadt S, Pengel D, Englert L, Bayer T and Wollenhaupt M 2018 Carrier-envelope-phase control of asymmetries in the multiphoton ionization of xenon atoms by ultrashort bichromatic fields *Phys. Rev. A* **97** 063402

[48] Cohen-Tannoudji C, Diu B and Laloe F 1991 *Quantum Mechanics* vol 2 (Berlin: Wiley)

[49] Lambropoulos P and Teague M R 1976 Two-photon ionization with spin–orbit coupling *J. Phys. B: At. Mol. Phys.* **9** 587